

Pulsed-field separation of particles in a microfluidic device

J. Regtmeier¹, R. Eichhorn², T.T. Duong¹, P. Reimann^{2,a}, D. Anselmetti¹, and A. Ros¹

¹ Experimental Biophysics & Applied Nanosciences, Bielefeld University, 33615 Bielefeld, Germany

² Theoretical Physics, Bielefeld University, 33615 Bielefeld, Germany

Received 2 February 2007

Published online: 11 May 2007 – © EDP Sciences, Società Italiana di Fisica, Springer-Verlag 2007

Abstract. We demonstrate the proof-of-principle of a new separation concept for micrometer-sized particles in a structured microfluidic device. Under the action of externally applied, periodic voltage-pulses two different species of like-charged polystyrene beads are observed to simultaneously migrate into opposite directions. Based on a theoretical model of the particle motion in the microdevice that shows good agreement with the experimental measurements, the underlying separation mechanism is identified and explained. Potential biophysical applications, such as cell sorting, are briefly addressed.

PACS. 85.85.+j Micro- and nano-electromechanical systems (MEMS/NEMS) and devices – 05.40.-a Fluctuation phenomena, random processes, noise, and Brownian motion – 05.60.-k Transport processes – 82.70.Dd Colloids

1 Introduction

Microfluidic analysis attracts more and more attention and gains significant importance in separation sciences. After the first proof-of-principle of microchip capillary electrophoresis in the early 1990s [1], a variety of separation problems have been addressed in microfluidic systems [2] and realized in various materials, accessible through the advances in microtechnology and microfabrication. Examples for successful transfer of common separation principles to the microchip format include biologically relevant methods such as cell sorting or cytometry [3], or electrophoretic protein and DNA separation [4]. Electrophoretic DNA separation turned out to become difficult for DNA-length above ≈ 40 kbp [5]. In this case separation performance is usually improved by pulsed-field techniques.

On the other hand, successful separations of DNA fragments >40 kbp in artificially structured microfluidic environments have been reported for micro- [6] and nanopillar [7] arrays as well as for magnetic bead [8] or nanosphere matrices [9]. Only recently, the first gel-free protein separation has been demonstrated based on a nanofilter array chip in which proteins are separated by a molecular sieving mechanism [10].

It has become clear that micro- and nanofluidic components offer a much broader and more complex horizon than originally expected by just scaling down conventional macroscopic analytical technologies. Completely new separation principles have been developed, that often make direct use of the thermal fluctuations (Brownian

motion) in the nano- or micrometer-scale devices. The benefits of this “noise” are unraveled only since recently with so-called Brownian ratchets [11] as the most prominent examples of this strategy. Ratchet effects have been applied to the transport of colloidal particles [12] and biomolecules [13–15]; DNA ratchets have been used for continuous-flow separation [15] and their application for single-nucleotide polymorphism genotyping has been anticipated [14]. Other examples are entropic traps [16], steric effects in geometrically structured microdevices [17], and deterministic separation in carefully tailored microstructures [18]. These techniques impressively demonstrate efficient alternatives for the tedious separation of large DNA (>40 kbp) in conventional slab gel format.

In this contribution, we focus on a new sorting and fractionation method for colloidal particles, utilizing thermal fluctuations in a periodically structured microfluidic device. The device is operating under non-equilibrium conditions that are created by an externally applied, periodically pulsed field with a non-vanishing average component. Here, we experimentally and theoretically show that colloidal particles in that device either move into the direction of the average force or else *opposite* to that force, depending on pulse amplitudes and durations and on particle properties. The latter phenomenon is known as absolute negative mobility, and has recently been reported to occur for colloidal particles in structured microfluidic systems [19]. By demonstrating that this paradoxical migration behavior can coexist with “normal” migration (i.e. motion in the direction of the average force) under identical experimental conditions, two different particle sorts are simultaneously moved into opposite directions. We

^a e-mail: reimann@physik.uni-bielefeld.de

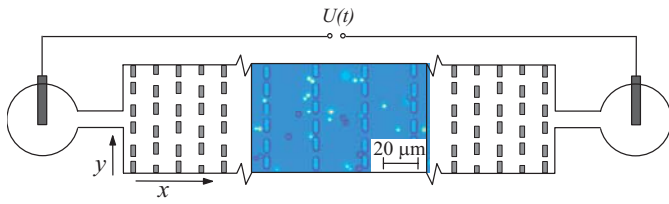


Fig. 1. Schematic top view (x - y plane) of the experimental setup (not to scale). Two reservoirs are connected by inlet and outlet channels with the central, microstructured part. The microstructure consists of periodically arranged rows of posts (obstacles, $3.1 \mu\text{m} \times 6.1 \mu\text{m}$) with a row-to-row distance of $(22.5 \pm 0.1) \mu\text{m}$. The enlargement in the middle shows a partial view (optical micrograph image) of the posts (bright rectangles) and two different species of migrating microbeads with diameters $1.9 \mu\text{m}$ (bright due to fluorescence) and $2.9 \mu\text{m}$ (dark dots, not fluorescent), see also Table 1. In each row of posts the gaps are alternately smaller $[(1.7 \pm 0.1) \mu\text{m}]$ and larger $[(3.1 \pm 0.1) \mu\text{m}]$ than the beads. Along the x -axis, the gaps are in line and again alternately large and small (see also Appendix A). Electrodes are immersed into the two reservoirs, and a time-dependent voltage $U(t)$ is applied to the electrodes (see Fig. 3).

discuss the potential of this separation tool for sorting, fractionation and separation of cells, cell components or biomolecules.

2 Experimental set-up and theoretical model

The main component of our microfluidic device fabricated in poly(dimethylsiloxane) (PDMS) is its topographically structured middle section with periodically arranged rows of rectangular posts separated by alternating small and large gaps, see Figure 1. Through inlet and outlet channels that merge into two reservoirs it is filled with a suspension of polystyrene microbeads at low concentration so that particle-particle interactions are negligible. Time-dependent electric fields can be applied along the x -axis via electrodes that are immersed in the reservoirs. Particle diameters and gap widths have been chosen such that the beads can pass through the large gaps but not through the small ones (see Fig. 1 and also Tab. 1). Microbead migration in our device is recorded by video microscopy and bead velocities are determined by optical particle tracking (see Appendix A).

Theoretically, we model the motion of a bead with coordinates $\mathbf{r} = (x, y, z)$ by the stochastic dynamics

$$\gamma \dot{\mathbf{r}} = \mathbf{F}(\mathbf{r}) + q \mathbf{E}_*(\mathbf{r}) U(t)/U_* + \boldsymbol{\xi}(t), \quad (1)$$

where $\mathbf{r} = \mathbf{r}(t)$, inertia effects are neglected (overdamped dynamics), and γ denotes the viscous friction coefficient [11,20]. The force field $\mathbf{F}(\mathbf{r})$ derives from an effective hard-wall potential of the microstructure (incorporating the finite particle radius), while $q \mathbf{E}_*(\mathbf{r})$ is the electrophoretic force on the bead generated by a constant reference voltage $U_* = 1 \text{ V}$, and $U(t)$ is the actual voltage

Table 1. “Free” particle velocity v_0 when applying a constant reference voltage $U_* = 1 \text{ V}$ to the electrodes in Figure 1 and diffusion coefficient D of the microbeads measured within the microstructure between two neighboring rows of posts.

Diameter [μm]	v_0 [$\mu\text{m/s}$]	D [$\mu\text{m}^2/\text{s}$]
1.9	0.28 ± 0.03	0.131 ± 0.005
2.9	0.14 ± 0.01	0.082 ± 0.007

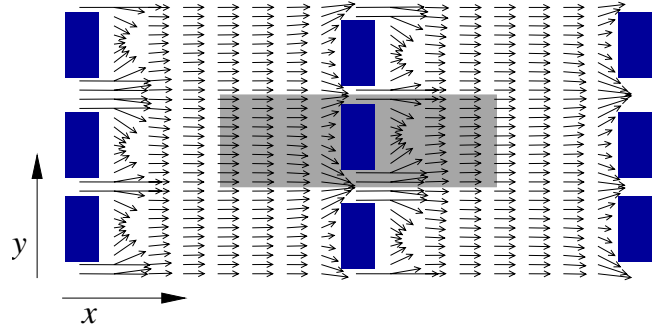


Fig. 2. Electric field in the microstructure (the obstacles are represented by blue rectangles) due to a (positive) constant voltage applied to the electrodes, see Figure 1. The grey region corresponds to the “central unit cell” that is periodically continued to obtain the electric field $\mathbf{E}_*(\mathbf{r})$ in equation (1) and that has also been used to create this picture (see also main text). Though the field is spatially inhomogeneous, its x -component always points in the same direction, i.e. the force on the particle always has an x -component in the same direction as the applied voltage [23].

applied to the electrodes in Figure 1. Thermal fluctuations are modeled as usual [11,20] by $\boldsymbol{\xi}(t) = (\xi_x(t), \xi_y(t), \xi_z(t))$, where $\xi_\alpha(t)$, $\alpha \in \{x, y, z\}$ are independent, unbiased Gaussian noise sources, satisfying the fluctuation dissipation relation $\langle \xi_\alpha(t) \xi_\alpha(t') \rangle = 2\gamma k T \delta(t - t')$, with Boltzmann’s constant k and room temperature $T \approx 290 \text{ K}$.

To determine the electric field $\mathbf{E}_*(\mathbf{r})$ in (1), we solved Laplace’s equation with periodic boundary conditions along the y -axis (cf. Fig. 1); along the x -axis, a preset potential difference over several spatial periods was imposed and the resulting “central unit cell” periodically continued. Moreover, assuming that the buffer solution is a perfect (electric) conductor and the microstructure (PDMS) is a perfect insulator, Neumann boundary conditions were adopted at the borders between microstructure and buffer. By this procedure, the relevant force field $q \mathbf{E}_*(\mathbf{r})$ in (1) can be determined up to an unknown gauge factor between experimental and theoretical potential differences. Typical results are illustrated by the grey arrows in Figure 2.

In equation (1), γ represents the effective coupling to the thermal environment and q that to the electric field, quantifying the above mentioned gauge factor. They depend in a very complex way on the geometry and the chemical surface properties of microstructure and bead, as well as on the electrohydrodynamic buffer properties. To determine q and γ quantitatively, we experimentally

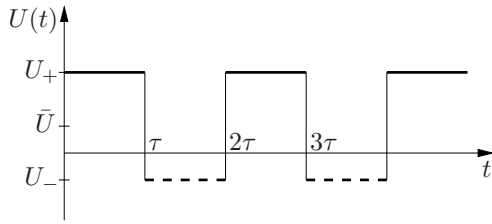


Fig. 3. Periodic voltage pulse used for particle separation in the device of Figure 1. The voltage switches periodically between $U_+ > 0$ V and $U_- < 0$ V with period 2τ and has an average component $\bar{U} := (U_+ + U_-)/2$. For symmetry reasons we can focus on $\bar{U} > 0$ V, i.e. $|U_+| > |U_-|$.

measured the voltage-dependent particle velocity v_0 in x direction as well as the diffusion coefficient D of the beads in the x - y -plane between two subsequent rows of posts in the microstructure by real-time bright field and fluorescence microscopy and averaging over a large number of particles, see Table 1. Then these experimental measurements were reproduced by the model dynamics (1) with fit parameters γ and q .

It is noteworthy that in the context of electrophoresis, q in (1) represents an effective charge only in a very loose sense [21]. These subtleties are automatically accounted for by our above fit of the relevant effective q . Similarly, the (quite small) electroosmotic effects are also effectively encapsulated in our q thanks to the similitude between electrophoresis and electroosmosis demonstrated in [22].

3 Particle separation under pulsed-field conditions

For simultaneous separation of two different particle species, the microfluidic device is driven by a pulsed voltage $U(t)$ with pulses of equal duration τ but different amplitudes $U_+ > 0$ V and $U_- < 0$ V (see also Fig. 3) [23]. This voltage signal thus has a non-vanishing average component $\bar{U} = (U_+ + U_-)/2$. In Figure 4, the average migration velocity

$$v := \left\langle \lim_{t \rightarrow \infty} \frac{x(t) - x(0)}{t} \right\rangle \quad (2)$$

of the two bead types is shown for different values of \bar{U} but with fixed $U_+ - U_-$. Due to symmetry reasons we restrict ourselves to $\bar{U} > 0$ V, i.e. $|U_+| > |U_-|$. For the experimental measurements (symbols with error bars), the long-time- and ensemble-average in (2) was approximated by observing about 40 microbeads over 3 to 4 periods of the driving $U(t)$ via real-time video microscopy (see Appendix A). Moreover, exploiting the symmetry of the microstructure (see Fig. 1), two independent measurements for each \bar{U} -value have been performed, one for the shown positive \bar{U} and one for the corresponding negative \bar{U} ; both measurements have been summarized in Figure 4. The two particle species could be simultaneously observed and distinguished by exploiting their different fluorescence properties, see inset of Figure 1. The theoretical curves are

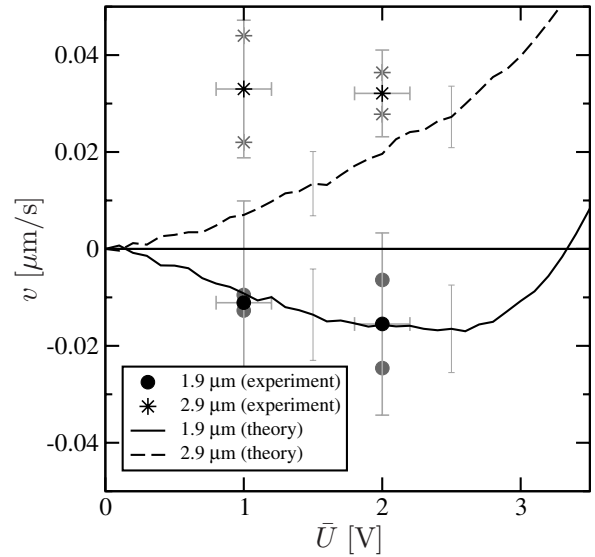


Fig. 4. Simultaneously observed average particle velocities for the two particle species from Table 1: the $1.9 \mu\text{m}$ -beads (dots) move into the direction opposite to \bar{U} , whereas the $2.9 \mu\text{m}$ -beads (stars) follow the direction of the average \bar{U} . The applied voltage $U(t)$ has constant “pulse distance” $U_+ - U_- = 12$ V, but varying average component $\bar{U} = (U_+ + U_-)/2$; the switching time is $\tau = 70$ s. The grey symbols result from two independent measurements, the first one performed for the indicated values $\bar{U} > 0$ V and, exploiting the symmetry of our device (see Fig. 1), the second one for the corresponding negative \bar{U} ; their average is shown with the black symbols with error bars. The curves result from numerical simulations of (1) for the two particle species. The error bars along the curves are theoretical estimates of the statistical uncertainties under the given experimental conditions. (Since their dependence on \bar{U} is very weak, only a few representative examples are shown.)

computed from numerical simulations of (1) with two sets of model parameters γ and q for the two different particle species that have been determined previously by the procedure described above (see also Tab. 1). Also shown in Figure 4 are the theoretically expected statistical fluctuations, obtained by numerical simulations for the same number of beads and observation times as in the experiment. The somewhat larger experimental errors can be explained by deviations from strictly spatially periodic conditions of the microstructure and bead-to-bead variations of size and surface charge. Within the experimental uncertainty, the agreement between theory and measurements is very good.

The remarkable feature of the results in Figure 4 is the qualitatively different average migration behavior of the two particle sorts under identical experimental conditions: while the $2.9 \mu\text{m}$ particles follow the direction of the average force [23], the $1.9 \mu\text{m}$ particles at the same time run into the direction opposite to that force. Typical particle trajectories illustrating this contrary behavior are shown in Figure 5.

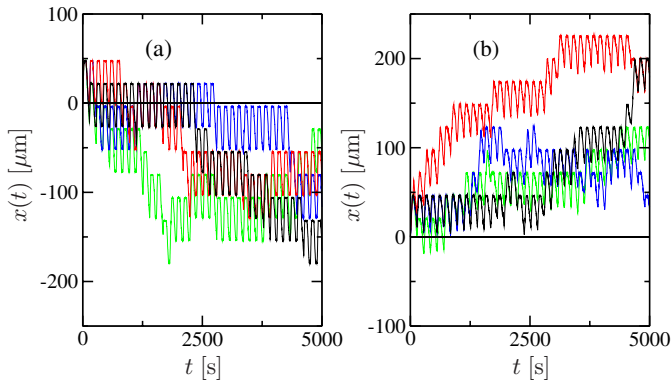


Fig. 5. Typical particle trajectories obtained from simulations of (1), illustrating the different migration behavior of the two particle species from Table 1 under the experimental conditions specified in Figure 4 at $\bar{U} = 2\text{ V}$. (a) $1.9\ \mu\text{m}$ -particles; (b) $2.9\ \mu\text{m}$ -particles.

4 Separation mechanism

In order to understand the physical mechanism behind this separation effect, we start by noting that the particles are larger in diameter (see Tab. 1) than the small gaps between the posts, such that these gaps together with the electric field act as particle “traps”. Deterministically, the pulsed field of Figure 3 would thus lead to a periodic particle motion in x direction back-and-forth between two such traps, always passing a large gap in the row of posts midway between the traps. Due to the thermal noise the particle laterally diffuses in y direction during its motion between two successive rows of posts (the effect of the diffusion in x direction is negligible) and so can avoid the gaps on its way in x direction. The combined effect of the back-and-forth motion (visible in the zig-zag course of the trajectories in Fig. 5) and the lateral diffusion is a net particle displacement in x direction. This is illustrated in Figure 6 by the four possible paths that lead to a net displacement of one obstacle row in positive or negative x direction by avoiding one gap during one driving period of the pulsed field.

The probability for avoiding a gap is notably different from zero only if the traveling time from one row of posts is not too small such that the diffusive dispersion during this time becomes sufficiently large. In other words, the probability for avoiding a gap is larger for smaller (in modulus) applied voltages. Obviously, it is also larger for smaller gaps because then the lateral size of the “basin of attraction” of the gap is smaller. We can infer that in the case $|U_+| > |U_-|$ out of the four migration processes in Figure 6 the process (D) occurs most frequently, whereas process (B) is the rarest one.

This conclusion seems to be completely independent of particle properties. However, it is tacitly assumed for each process in Figure 6 that the particle can pass at least that number of obstacle rows along the x direction during the pulse duration τ which is required for the specific process to occur. For instance, for process (D) the particle must be able to proceed at least by two obstacle rows in order

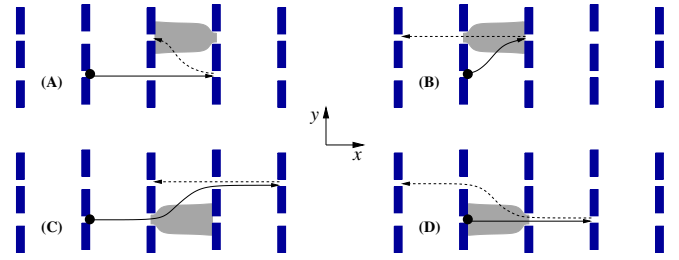


Fig. 6. Sketches of typical particle trajectories in the microstructure of Figure 1 (blue rectangular obstacles), where the particle avoids one gap during a driving period 2τ of the pulsed field (see Fig. 3); the starting positions are marked by the black “beads”. The solid and dashed arrows correspond to the motion during the U_+ - and U_- -phases of the pulsed field in Figure 3. (A, B): The particle avoids *the first large gap* by entering the “attraction basin” (grey region) of an adjacent small gap due to lateral diffusion; this occurs during the U_- -pulse in (A) and during the U_+ -pulse in (B). (C, D): The particle passes through the large gap, but then avoids *the small gap* by diffusively leaving its “attraction basin” (grey region); this occurs during the U_+ -pulse in (C) and during the U_- -pulse in (D). The grey-shaded deterministic “attraction basins” of the traps are obtained from closer inspection of the electric field in Figure 2. The processes (A) and (C) yield a net displacement of one row distance in *positive* x direction, whereas in (B) and (D) the particle is moved by one row distance in *negative* x direction.

to reach the second large gap within the time τ when the voltage U_- is applied (see the dashed arrow). This yields the condition $\tau \gtrsim (LU_*)/(v_0|U_-|)$ or

$$\frac{v_0}{U_*} \gtrsim \frac{L/\tau}{|U_-|}, \quad (3)$$

where L is the spatial period of the microstructure along the x direction, i.e. for the device of Figure 1 we have $L = 51.2\ \mu\text{m}$, and U_* is the reference voltage at which v_0 has been measured (see Tab. 1 and Eq. (1)). For the remaining three processes in Figure 6 either the minimal required traveling distance is smaller (processes (A) and (B)) or this distance is the same as for process (D) but is traveled under the action of the larger voltage U_+ (process (C)). On the one hand the condition (3) thus guarantees the occurrence also of the (less frequent) processes (A), (B), (C), on the other hand these three processes still do occur if (3) is violated.

For the first particle species in Table 1 (with diameter of $1.9\ \mu\text{m}$) one finds that (3) is fulfilled under the experimental conditions specified with Figure 4 for $0\text{ V} < \bar{U} \lesssim 3\text{ V}$ (i.e. $-6\text{ V} < U_- \lesssim -3\text{ V}$). Hence, the most probable migration process of Figure 6, i.e. process (D) with a net displacement in the direction opposite to the average voltage \bar{U} , dominates the migration behavior of this particle species, explaining why it has a *negative* average velocity in Figure 4. In contrast, the second particle species of Table 1 (with diameter of $2.9\ \mu\text{m}$) does not fulfill the condition (3), such that the dominating migration

processes of Figure 6 are (A) and (C), leading to a *positive* average velocity in Figure 4.

As a final remark, we address our restriction in Figure 6 to paths with just one avoided gap per period of the pulsed field. There are also processes where several gaps are avoided within a driving period, usually yielding net displacements of several obstacle rows in positive or negative x direction. E.g., once the particle succeeded in avoiding the small gap (trap), it may again succeed in avoiding the next small gap instead of being trapped there like in Figures 6(C) or 6(D), and so on. Such processes are, however, considerably less likely than those of Figure 6. E.g., the probability for avoiding n traps in a row quickly decreases with the probability for avoiding one trap to the power of n [24]. Moreover, for multiple gap avoidances the particle must be able to travel larger distances in x direction during the time intervals with constant U_{\pm} , and thus longer pulse durations τ than the one used here would be required. In summary, paths with several avoided gaps can safely be neglected in our above qualitative discussion. This conclusion is also supported by the particle trajectories shown in Figure 5.

5 Conclusion

We have demonstrated the proof-of-principle of a new method for selectively and simultaneously steering different (like-charged) particle species into opposite directions in a microfluidic device (see Fig. 4). The separation effect is based on the interplay of externally applied periodic voltage-pulses $U(t)$ (cf. Fig. 3) with the ambient thermal noise, such that the particle can diffusively avoid particle traps in the microstructure (cf. Fig. 1), and, as a consequence, either runs into the direction opposite to the non-vanishing average component \bar{U} of the pulsed voltage (cf. Fig. 3) or else follows the direction of \bar{U} , depending on the condition (3). The resulting average particle velocity is opposite to \bar{U} for particle species that fulfill (3) and is in the direction of \bar{U} if (3) is violated. Note that the separation criterion (3) depends on parameters of the externally applied voltage-pulse $U(t)$, such that the “operation mode” of the microfluidic device can easily be adapted to a given separation task by suitably tailoring $U(t)$.

This selective transport mechanism opens up interesting new perspectives for efficient and flexible separation of micrometer-sized colloidal particles, but also biological compounds of comparable size, like cells or cell organelles. Moreover, this mechanism may be straightforwardly exploited for continuous-flow separation, e.g. by adding perpendicular injection channels in the middle of the structured region of our device (see Fig. 1), through which a particle solution could be delivered continuously; the sorted constituents could then be collected at two outlets at the left and right end of the microstructure.

Interestingly, the presented phenomenon is based on the existence of noise, on the other hand, its main limiting factor so far is the *weakness* of the thermal noise, being responsible for the prohibitively slow average velocities observed in our proof-of-principle experiment (see Fig. 4).

Specifically, as compared to the deterministic separation technique put forward by Huang *et al.* in reference [18], our present method is still substantially slower. Hence, the natural next step we are presently pursuing is to strengthen the relative importance of thermal noise by optimizing the geometry of the microstructure and/or by employing smaller particles. While our present method benefits from the unavoidably increasing noise effects for decreasing particle size, the deterministic concept of Huang *et al.* [18] will become less and less effective.

An even more interesting — but also more challenging — extension will be to replace the colloidal particles by single biomolecules like DNA and globular proteins. To selectively control the transport of these biomolecules, a substantial modification of the basic physical mechanism of our present work will be necessary. This issue is the subject of our ongoing investigations.

We gratefully acknowledge financial support by the Deutsche Forschungsgemeinschaft within the Collaborative Research Project 613 (project D2) and RE 1344/3-1.

Appendix A: Materials and methods

Chemicals and reagents. PDMS (Sylgard 184) was purchased from Spoerle Electronic (Germany), glass microscope slides from Menzel (Germany). Tween 20 and EDTA were obtained from Sigma (Germany). Disodium hydrogenphosphate dihydrate, T2-DNA, β -mercaptoethanol, sodium chloride, N-hydroxysuccinimide (NHS), N-(3-dimethylaminopropyl)-N'-ethyl-carbodiimide hydrochloride (EDC), and L-histidine were purchased from Fluka (Germany). The triblock copolymer Pluronic F-108 was a generous gift from BASF (Germany). For all solutions deionized water from a Milli-Q biocel (Millipore, USA) was used. Carboxyl modified polystyrene particles (CML microbeads) of 2.9 μm diameter as well as fluorescently stained CML beads of 1.9 μm diameter were obtained from Interfacial Dynamics Corporation (USA).

PDMS Devices. A master with the inverted relief of the microstructure was fabricated via spincoating a photoresist (SU-8) onto a Si-wafer, UV-exposing through a chromium mask and development in a developer bath. The detailed fabrication procedure was recently published [25]. The polymer Sylgard 184 and its curing agent were mixed in a 10:1 ratio and poured over the master wafer. After curing for 4 h, the crosslinked polymer was easily peeled off the wafer and the reservoir holes were punched. Before assembly, the microstructured PDMS slab and a PDMS coated glass slide were oxidized in a home built oxygen plasma chamber for 30 s. The microfluidic channels were coated with the 500 μM triblock copolymer F-108 in 100 mM phosphate buffer (pH = 8.3) for 18 h, significantly reducing adhesion of colloidal particles [26].

A schematic top view (x - y plane) of the experimental setup is depicted in figure 1. The two reservoirs of 2 mm diameter are connected by inlet and outlet channels (each of length 2500 μm and cross section 24 $\mu\text{m} \times 9 \mu\text{m}$)

with the central, microstructured part. It extends over $6000\ \mu\text{m} \times 400\ \mu\text{m}$ in the x - y plane and $9\ \mu\text{m}$ in height (z direction) and contains periodically arranged posts (obstacles, $3.1\ \mu\text{m} \times 6.1\ \mu\text{m}$). In each row of posts the gaps are alternately smaller [$(1.7 \pm 0.1)\ \mu\text{m}$] and larger [$(3.1 \pm 0.1)\ \mu\text{m}$] than the beads. The row distance is $(22.5 \pm 0.1)\ \mu\text{m}$. Along the x -axis, the gaps are in line and again alternately large and small.

Detection. Particle movement was recorded on an inverted microscope (Axiovert 200, Zeiss, Germany) equipped with bright field and fluorescence detection as well as with an automatized x/y -stage (99S008, Ludl Electronic Products, USA) using a $\times 20$ objective (LD Achrom Plan 20x/0.40korr, Zeiss, Germany) and a sensitive CCD-camera (Sensicam, LaVision, Germany). The velocity of the colloidal particles was analyzed by particle image velocimetry (PIV) using ImageJ freeware and Plugin MTrack2 (Nico Stuurman, University of California, San Francisco).

Chip operations. Initial filling of the microchannel was performed by capillary action and application of vacuum to a reservoir. Electrical connection to the microchip device was achieved with platinum electrodes dipped into the reservoirs. DC and AC-voltages were applied using two power supplies from FUG (Model MCN 14-2000 and MCN 140-1250, Germany) and a relay circuit. Instrumental control and data acquisition were performed via software programmed in LabView (National Instruments, USA). Prior to microchip operations, butylamine was attached to the carboxyl groups on the surface of the $2.9\ \mu\text{m}$ -beads using a reactive carbodiimid. The microbeads were reacted with butylamine in a concentration of $89\ \text{mM}$ for $90\ \text{min}$ under continuous shaking with a Vortex in $100\ \text{mM}$ phosphate solution ($\text{pH} = 8.3$) containing $2.2\ \text{mM}$ NHS and $44\ \text{mM}$ EDC. For chip operations, CML beads (both $1.9\ \mu\text{m}$ and derivatized $2.9\ \mu\text{m}$) were diluted in $100\ \text{mM}$ phosphate buffer ($\text{pH} = 8.3$) containing $200\ \mu\text{M}$ Tween 20 and $100\ \mu\text{M}$ L-histidine and initially filled into the microchip by hydrodynamic flow.

References

- D.J. Harrison, A. Manz, Z. Fan, H. Lüdi, H.M. Widmer, *Anal. Chem.* **64**, 1926 (1992); D.J. Harrison, K. Fluri, K. Seiler, Z. Fan, C.S. Effenhauser, A. Manz, *Science* **261**, 895 (1993); K. Seiler, D.J. Harrison, A. Manz, *Anal. Chem.* **65**, 1481 (1993); C.S. Effenhauser, A. Manz, H.M. Widmer, *Anal. Chem.* **65**, 2637 (1993)
- D.R. Reyes, D. Iossifidis, P.A. Auroux, A. Manz, *Anal. Chem.* **74**, 2623 (2002); P.A. Auroux, D. Iossifidis, D.R. Reyes, A. Manz, *Anal. Chem.* **74**, 2637 (2002); T. Vilknær, D. Janásek, A. Manz, *Anal. Chem.* **76**, 3373 (2004)
- H. Andersson, A. van den Berg, *Sensors, Actuators B* **92**, 315 (2003); J. El-Ali, P.K. Sorger, K.F. Jensen, *Nature* **442**, 403 (2006)
- C.W. Kan, C.P. Fredlake, E.A.S. Doherty, A.E. Barron, *Electrophoresis* **25**, 3564 (2004); V. Dolnik, S. Liu, *J. Sep. Sci.* **28**, 1994 (2005)
- J.-L. Viovy, *Rev. Mod. Phys.* **72**, 813 (2000)
- O. Bakajin, T.A.J. Duke, J. Tegenfeldt, C.F. Chou, S.S. Chan, R.H. Austin, E.C. Cox, *Anal. Chem.* **73**, 6053 (2001); L.R. Huang, J.O. Tegenfeldt, J.J. Kraeft, J.C. Sturm, R.H. Austin, E.C. Cox, *Nature Biotechnol.* **20**, 1048 (2002); K. Inatomi, S. Izuo, S. Lee, H. Ohji, S. Shiono, *Microelectron. Eng.* **70**, 13 (2003)
- N. Kaji, Y. Tezuka, Y. Takamura, M. Ueda, T. Nishimoto, H. Nakanishi, Y. Horiike, Y. Baba, *Anal. Chem.* **76**, 15 (2004)
- P.S. Doyle, J. Bibette, A. Bancaud, J.-L. Viovy, *Science* **295**, 2237 (2002); N. Minc, C. Futterer, K. Dorfman, A. Bancaud, C. Gosse, C. Goubault, J.L. Viovy, *Anal. Chem.* **76**, 3770 (2004)
- M. Tabuchi, M. Ueda, N. Kaji, Y. Yamasaki, Y. Nagasaki, K. Yoshikawa, K. Kataoka, Y. Baba, *Nature Biotechnol.* **22**, 337 (2004)
- J. Fu, P. Mao, J. Han, *Appl. Phys. Lett.* **87**, 263902 (2005)
- P. Reimann, *Phys. Rep.* **361**, 57 (2002)
- J. Rousselet, L. Salome, A. Ajdari, J. Prost, *Nature* **370**, 446 (1994); L.P. Faucheux, A. Libchaber, *J. Chem. Soc. - Faraday Trans.* **91**, 3163 (1995); L. Gorre-Talini, J.P. Spatz, P. Silberzan, *Chaos* **8**, 650 (1998); C. Marquet, A. Buguin, L. Talini, P. Silberzan, *Phys. Rev. Lett.* **88**, 168301 (2002)
- J.S. Bader, R.W. Hammond, S.A. Henck, M.W. Deem, G.A. McDermott, J.M. Bustillo, J.W. Simpson, G.T. Mulhern, J.M. Rothberg, *Proc. Nat. Acad. Sci. USA* **96**, 13165 (1999)
- J.S. Bader, M.W. Deem, R.W. Hammond, S.A. Henck, J.W. Simpson, J.M. Rothberg, *Appl. Phys. A* **75**, 275 (2002)
- L.R. Huang, E.C. Cox, R.H. Austin, J.C. Sturm, *Anal. Chem.* **75**, 6963 (2003)
- J. Han, H.G. Craighead, *Science* **288**, 1026 (2000); J. Han, H.G. Craighead, *Anal. Chem.* **74**, 394 (2002)
- A. Ros, W. Hellmich, T. Duong, D. Anselmetti, *J. Biotechnol.* **112**, 65 (2004)
- L.R. Huang, E.C. Cox, R.H. Austin, J.C. Sturm, *Science* **304**, 987 (2004)
- A. Ros, R. Eichhorn, J. Regtmeier, T. Duong, P. Reimann, D. Anselmetti, *Nature* **436**, 928 (2005)
- N.G. van Kampen, *Stochastic Processes in Physics and Chemistry* (Elsevier, Amsterdam, 1992); H. Risken, *The Fokker-Planck Equation* (Springer, Berlin, 1989)
- D. Long, J.-L. Viovy, A. Ajdari, *Phys. Rev. Lett.* **76**, 3858 (1996)
- E.B. Cummings, S.K. Griffiths, R.H. Nilson, P.H. Paul, *Anal. Chem.* **72**, 2526 (2000)
- We adopt the sign convention that a positive voltage generates positive forces on the particles along the x -axis.
- R. Eichhorn, P. Reimann, P. Hänggi, *Phys. Rev. Lett.* **88**, 190601 (2002); R. Eichhorn, P. Reimann, *Acta Phys. Pol. B* **37**, 1491 (2006)
- T. Duong, G. Kim, R. Ros, M. Streek, F. Schmid, J. Brugger, D. Anselmetti, A. Ros, *Microelectron. Eng.* **67-68**, 905 (2003)
- W. Hellmich, J. Regtmeier, T. Duong, R. Ros, D. Anselmetti, A. Ros, *Langmuir* **21**, 7551 (2005)